

A few-layer graphene nanomechanical resonator driven by multifrequency digital signals

Received: 1 May 2024

Accepted: 18 October 2025

Published online: 04 December 2025

 Check for updatesCe Zhang^{1,2,3,4,5}, Heng Lu^{1,2,3,4,5} ✉, Chen Yang^{1,2,3,4,5}, YuBin Zhang^{1,2,3,4,5}, FengNan Chen^{1,2,3,4,5}, Ying Yan^{1,2,3,4,5} & Joel Moser^{1,2,3,4,5} ✉

Nanomechanical resonators driven by multifrequency signals merge mesoscopic vibration physics with radio communication technologies. Their fundamental property is resonant filtering: they respond only to driving signals with frequency components within their mechanical bandwidth. Compared to single-tone drives, multifrequency drives produce richer dynamics, with all frequency components transduced simultaneously into vibrations of varying amplitudes and phases that superimpose and interfere. Here, we employ a few-layer graphene nanomechanical resonator as a filter for broadband, digitally modulated video signals. We transduce the modulated signals into modulated vibrations and subsequently demodulate these into a nanomechanical video. This approach shows vibrational features that are absent in single-tone or noise-driven responses.

Nanomechanical resonators enable the study of mesoscopic vibrations within individual systems that can be tuned and controlled^{1–4}. Owing to their small masses, they transduce weak driving forces near resonance into vibrations of sizeable amplitude. Their frequency response resembles that of resonant tuning circuits in analogue radio receivers, with the force acting as the driving voltage and the mechanical displacement acting as the circuit charge. Just as the resonant frequency of an electrical circuit can be tuned using a variable capacitor or inductor, the resonant frequencies of the mechanical response, which are the frequencies of the vibrational modes, can be adjusted in situ using capacitive^{5,6} and dielectric forces⁷, or by straining the resonator either mechanically⁸ or through its thermal expansion^{9,10}. As in the electrical case, the frequency bandwidth of the mechanical response is governed by both dissipation and resonant frequency fluctuations³. A narrower electrical response enhances frequency selectivity, while a narrower mechanical response facilitates the sensing of smaller driving forces. A broader response can also be advantageous. For instance, a wide-bandwidth tuning circuit is required to isolate a modulated radio

signal and capture its full spectral content while filtering out signals in adjacent bands. Similarly, nanomechanical resonators with a large bandwidth W_m can respond to nearly resonant forces whose broad spectra are contained within the mechanical response^{11–14}. Such large-bandwidth resonators also enable the study of resonant frequency fluctuations induced far below resonance by fluctuators with correlation times as short as $1/W_m$ ^{15–20}. In essence, nanomechanical resonators function as tunable bandpass filters for nearly resonant forces and as detectors for nonresonant fluctuators.

While the nanomechanical response to broadband force noise and low-frequency fluctuators has been thoroughly studied, the response to multifrequency coherent drives has received comparatively less attention. In many cases where multifrequency signals are applied, only a single frequency component is used to measure the response, while the other components serve different purposes. For example, amplitude-modulated^{6,21,22} and frequency-modulated signals²³ have been employed to drive the resonator at the single frequency of the carrier, with the modulation sidebands used to detect the

¹School of Optoelectronic Science and Engineering, Soochow University, Suzhou, China. ²Collaborative Innovation Center of Suzhou Nano Science and Technology, Soochow University, Suzhou, China. ³Key Lab of Advanced Optical Manufacturing Technologies of Jiangsu Province, Soochow University, Suzhou, China. ⁴Key Lab of Modern Optical Technologies of Education Ministry of China, Soochow University, Suzhou, China. ⁵Jiangsu Key Laboratory of Flexible Optoelectronics and Micro-Nano Manufacturing, Soochow University, Suzhou, China. ✉ e-mail: luheng@suda.edu.cn; j.moser@suda.edu.cn; Joel.Moser@icfo.eu

vibrations. Two-tone signals, consisting of one tone near resonance and a second tone outside the response, have been employed to explore various vibrational phenomena. Examples abound and include pump-probe spectroscopy for measuring intermode coupling²⁴, parametrically induced mode coupling, used to heat or cool vibrations^{25–28} and to engineer nonlinear friction²⁹, and symmetry-breaking parametric resonators for binary information encoding^{30–32}. By contrast, applications involving multifrequency signals where the entire spectrum directly drives vibrations remain relatively limited. Two-tone drives have been used to demonstrate signal mixing with nonlinear nanomechanical resonators^{33,34}. The interplay between a near-resonant two-tone drive and parametric pumping has enabled the realization of mechanical logic gates³⁵. A combination of strong and weak near-resonant tones has been shown to squeeze thermomechanical noise³⁶. Resonators driven nonlinearly by two strong tones near resonance have exhibited unconventional dynamics, where the beating between the tones acts as a slow modulation of the bifurcation points^{37,38}. Overall, studying nanomechanical resonators driven by multifrequency signals sheds light on the physics of mesoscopic vibrations and leads to proof-of-concept demonstrations for potential applications.

Appealing demonstrations of the physics of multifrequency vibrations are provided by nanomechanical radio receivers and transmitters for frequency modulated (FM) signals^{39,40}. Nanomechanical FM receivers have been realized using suspended nanotubes^{23,41–43} and nanomachined silicon tuning forks⁴⁴. The FM voltage waveform is capacitively coupled to the receiving resonator, creating a modulated driving force that the resonator passively responds to. By contrast, nanomechanical FM transmitters output a modulated radio-frequency signal. These have been demonstrated using suspended graphene⁴⁵ and nanomachined polysilicon disks^{46,47}. In these devices, the vibrating element forms part of an electrical positive feedback loop that sustains self-oscillations. The oscillation frequency is modulated by a stream of low-frequency voltage pulses or by an audio waveform, which induces a slowly varying capacitive force between the oscillator and a nearby electrode, thereby slowly modulating the spring constant. This approach, akin to “keying” the baseband components of the vibrations, is reminiscent of Morse code telegraphy. In summary, nanomechanical radio receivers and transmitters illustrate the richness of mesoscopic vibrations driven by multifrequency signals. By producing an audible copy of these vibrations, they also appeal to science and technology enthusiasts.

Here, we demonstrate that nanomechanical resonators based on few-layer graphene (FLG) can transduce a multifrequency, digital video signal into modulated vibrations that encode an accurate copy of the video. We quantify the transduction using standard signal quality metrics for digital communications. We have chosen FLG resonators for their large resonant frequency tunability within the high-frequency (HF) and the very-high-frequency (VHF) bands of the radio spectrum, and for the compromise they offer between broad bandwidths and moderate force sensitivities. A key point in our study is that the signal bandwidth is larger than or comparable to that of the mechanical response. This contrasts with nanomechanical radio receivers and transmitters discussed above, which process audio baseband signals with bandwidths much smaller than the mechanical bandwidth. A wide-bandwidth coherent drive serves as an effective probe for exploring the physics of the mechanical response. Because the resonator behaves as a filter, it shapes the multifrequency driving signal and transduces it into multifrequency vibrations with different phases and amplitudes that superimpose and interfere. We find that these interferences have a profound impact on the signal-to-noise ratio and on the bit error ratio of the transduction. We theoretically model the response to our multifrequency drive and successfully reproduce our experimental data. We establish a relation between the mechanical bandwidth and the maximum signal bandwidth that can be transduced without information loss in the baseband components of the vibrations. Our work

contributes to the recent study of resonators driven nonlinearly by multiple tones. Whereas earlier studies explored the case of two-tone driving^{37,38}, we investigate a previously unexplored regime in which the resonator is coherently driven by a near continuum of frequency components across its full mechanical bandwidth. We also envision experimental applications in the context of renewed interest in HF and VHF band communications⁴⁸. Even though data rates in these bands are low, HF and VHF remain among the most robust and reliable options for long-distance communication in scenarios where other channels are unavailable. Future HF communication systems may be required to transmit and receive weak signals encoded with compressed images or videos⁴⁸, while narrowband digital television has already been demonstrated in the VHF band⁴⁹. Our results suggest that nanomechanical resonators could serve as passive receivers for such signals, just as they do for audio-modulated radio waves.

Results

We begin by briefly describing the principle of our measurements. Our experimental setup is shown in Fig. 1a. The FLG resonator, estimated from its optical contrast to be composed of ~10 layers, is shaped as a 3 μm diameter drum suspended over a local gate electrode (Supplementary Note 1). It is kept at room temperature in a vacuum enclosure and held by a piezo positioner. Two similar devices have been measured, yielding comparable results. Homemade flexible transmission lines, fabricated from copper-clad ribbons of Kapton, deliver radio-frequency signals to the gate without impeding the motion of the positioner^{50,51}. With the resonator grounded, the voltage waveform incident on the gate, $s(t)$, creates a capacitive force $F_d(t) \simeq (1 + \Gamma)C'_g V_g^{dc} s(t)$, where $\Gamma \simeq 1$ is the reflection coefficient at the gate, C'_g is the derivative of the capacitance between the resonator and the gate with respect to displacement along the out-of-plane \hat{z} -direction (Fig. 1a), V_g^{dc} is a dc voltage applied to the gate, and t is time. Near resonance, $F_d(t)$ drives flexural vibrations along \hat{z} . To measure these vibrations, we place the resonator in an optical standing wave formed between the gate and a quarter-wave plate⁵², a standard configuration for studying two-dimensional resonators^{1,53–56}. The amount of optical energy absorbed by the resonator from the standing wave is modulated at the frequency of the flexural vibrations, resulting in oscillations in the output voltage of a photodetector placed in the path of the reflected light⁵⁴.

The originality of our setup lies in our technique to create a modulated drive and demodulate the nanomechanical response. The baseband signal of the drive is built from a video in MP4 format, which we convert into a video Transport Stream (TS). The TS data stream is split into two bit streams that are used to associate each symbol in the baseband signal with 2 bits. We implement a 4-quadrature amplitude modulation scheme (4-QAM, equivalent to quadrature phase shift keying). In this scheme, each symbol is represented by two nearly simultaneous voltage pulses, $I_{in} = V_{in}p$ and $Q_{in} = V_{in}q$, with V_{in} a voltage and $p = \pm 1$, $q = \pm 1$ (vertical bars in Fig. 1b). These pulses are filtered using a root raised cosine (RRC) filter, producing two smoothly varying signals, $\tilde{I}_{in}(t)$ and $\tilde{Q}_{in}(t)$. This filter both minimizes intersymbol interference (when paired with a matched RRC filter at the receiver) and ensures that the resonator is driven by a slowly modulated waveform. Without this filtering, the resonator would attenuate much of the information encoded in the high-frequency components of the pulses. The signals $\tilde{I}_{in}(t)$ and $\tilde{Q}_{in}(t)$ modulate the amplitude of the in-phase and quadrature components of the driving waveform, $s(t) = \tilde{I}_{in}(t) \cos(2\pi f_d t) + \tilde{Q}_{in}(t) \sin(2\pi f_d t)$, where f_d is the carrier (drive) frequency (Supplementary Note 2). Both baseband modulation (bit-to-symbol mapping) and carrier modulation of $s(t)$ are implemented using GNU Radio, an open-source software development toolkit for signal processing⁵⁷. The resulting waveform $s(t)$ is converted into an analog signal using a low-cost software-defined radio (SDR) transmitter (HackRF One by Great

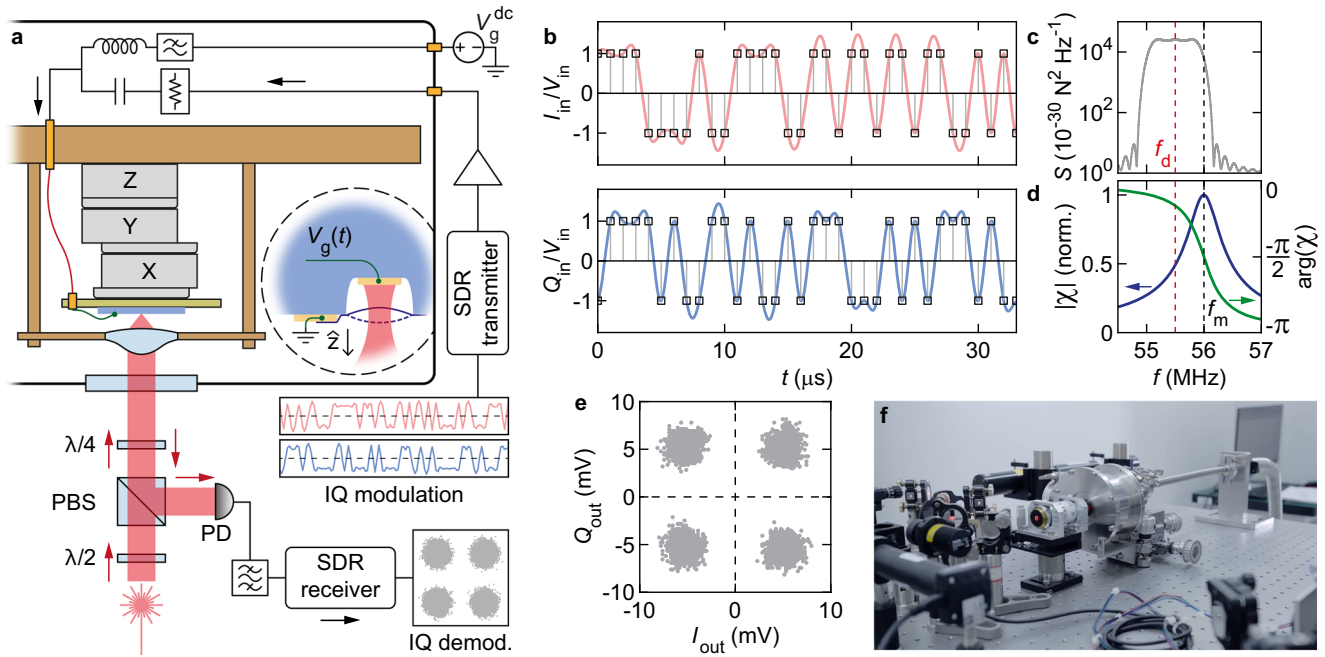


Fig. 1 | Principle of the experiment. **a** Experimental setup. XYZ: piezo positioner. Red wavy line: flexible transmission line. $V_g(t) = V_g^{dc} + s(t)$. PBS: polarizing beam splitter. $\lambda/2$, $\lambda/4$: half-, quarter-wave plates. An aspheric lens focuses incident light (wavelength ≈ 633 nm) onto the resonator and collects light reflected by the gate⁵⁰. SDR: software-defined radio. “IQ modulation” represents two experimental streams of filtered voltage pulses forming one symbol stream. Black (red) arrows indicate the propagation direction of radio frequency (optical) waves. **b** Computed voltage pulse streams before (vertical bars ending in squares) and after (red and blue wavy traces) convolution with a raised cosine (RC) filter. Symbol rate

$R_{\text{sym}} = 10^6$ Hz. **c** Averaged power spectral density of the driving force $S(f)$ as a function of spectral frequency, calculated using an RC filter, for drive power at the gate $P_d = -31$ dBm and $R_{\text{sym}} = 10^6$ Hz. $S(f)$ is superimposed on the background of thermal forces. **d** Magnitude and phase of the linear mechanical response χ , calculated for a mechanical quality factor $Q_m = 100$. **e** Constellation diagram of I_{out} and Q_{out} , the in-phase and quadrature components of the decimated baseband signal at the photodetector output. Source data are provided as a Source Data file. **f** Frame from a nanomechanically processed video reconstructed from I_{out} and Q_{out} .

Scott Gadgets⁵⁸). The calculated power spectral density S of the driving force $F_d(t)$, averaged over multiple realizations, is shown in Fig. 1c as a function of spectral frequency f . We consider a drive power at the gate $P_d = 10 \log_{10}[(1 + \Gamma^2 \langle s^2(t) \rangle) / (50 \times 10^{-3})] \approx -31$ dBm, where $\langle \cdot \rangle$ denotes time averaging. We set $V_g^{dc} = 13$ V and estimate $C_g \approx 9 \times 10^{-10}$ F m⁻¹ with COMSOL. The spectrum $S(f)$ is centered at f_d and spans a full bandwidth $W \approx 1.3R_{\text{sym}}$, where $R_{\text{sym}} = 10^6$ Hz is the symbol rate and 1.3 accounts for the filter roll-off factor. The area under $S(f)$ corresponds to the variance of $F_d(t)$, which depends only on the drive amplitude and is independent of R_{sym} . Importantly, $F_d(t)$ is not a delta-correlated noise but rather a coherent waveform (Supplementary Note 2). Figure 1d shows the normalized magnitude and the phase of the linear mechanical response. The bandwidth of the drive W exceeds the resonator’s mechanical bandwidth $W_m = f_m/Q_m \approx 0.56 \times 10^6$ Hz, where $f_m \approx 56 \times 10^6$ Hz is the resonant frequency of the fundamental mode and $Q_m \approx 100$ is its quality factor.

To measure the voltage $v(t)$ at the output of the photodetector, we use a low-cost SDR receiver (NESDR Smart by Nooelec⁵⁸) that downconverts the signal to baseband. Using GNU Radio, we correct transmission delays with a polyphase filter bank^{59,60} and apply matched filtering using an RRC filter. This yields the in-phase and quadrature components of the received signal, expressed as $v(t) = \hat{I}_{\text{out}}(t) \cos(2\pi f_d t) + \hat{Q}_{\text{out}}(t) \sin(2\pi f_d t)$. We decimate $\hat{I}_{\text{out}}(t)$ and $\hat{Q}_{\text{out}}(t)$ at the symbol rate R_{sym} to obtain the discrete symbol components I_{out} and Q_{out} . These values, acquired for 2 s, are plotted on a constellation diagram in Fig. 1e. This diagram helps visualize the process of converting symbols back into bits, the decision to ascribe a received symbol to a pair of bits depending on which quadrant the symbol appears in⁶¹. The GNU Radio flowcharts used for modulation and demodulation are provided in Supplementary Note 3. Finally, Fig. 1f shows a frame from a nanomechanical video obtained by

converting the I_{out} and Q_{out} streams back into an MP4 video using FFmpeg, an open-source multimedia processing tool⁶². The frame shows an early configuration of our setup, featuring an optical objective outside the vacuum enclosure.

Obtaining a nanomechanical video requires optimizing the drive power P_d , the drive frequency f_d , and the symbol rate R_{sym} . We vary these parameters individually and monitor their impact on the constellation diagram of the demodulated outputs I_{out} and Q_{out} . As f_d is stepped through resonance, the constellation diagram undergoes significant changes that are best visualized as animations (Supplementary Movie 1 shows diagrams measured as f_d is increased at various P_d values, with $R_{\text{sym}} = 0.5 \times 10^6$ Hz). A simple metric we extract from the constellation diagram is the time-averaged length of the I – Q vector in one quadrant, defined as $L = \langle |I_{\text{out}} + iQ_{\text{out}}| \rangle$. The spread of the symbol clouds (Fig. 1e) also contains useful information. We quantify it within a single quadrant as $d = \langle (I_{\text{out}} - \langle I_{\text{out}} \rangle)^2 + (Q_{\text{out}} - \langle Q_{\text{out}} \rangle)^2 \rangle^{1/2}$. The logarithmic ratio, $\varepsilon = 20 \log_{10}(L/d)$, can be interpreted as a signal-to-noise ratio, since noise at the output of the receiver and the dephasing of vibrations by the mechanical response both contribute to the spread d . In digital communications, ε is known as the reciprocal of the error vector magnitude of the symbols. Larger values of ε indicate better symbol separation and correspond to smoother video playback.

Measurements of $L(f_d)$ and $\varepsilon(f_d)$ are shown as dots in Fig. 2a–d and Fig. 2e–h, respectively, for several values of P_d at $R_{\text{sym}} = 0.5 \times 10^6$ Hz (the minimum values of L and ε required for successful video decoding are given in Supplementary Note 4). Similar measurements at $R_{\text{sym}} = 10^6$ Hz are presented in Fig. 3. In all measurements, we set $V_g^{dc} = 13$ V, corresponding to a mechanical resonant frequency $f_m \approx 56 \times 10^6$ Hz. For both symbol rates, the lineshapes of $L(f_d)$ broaden and become increasingly asymmetric as P_d increases, consistent with the onset of nonlinearities in the mechanical response. While the $L(f_d)$

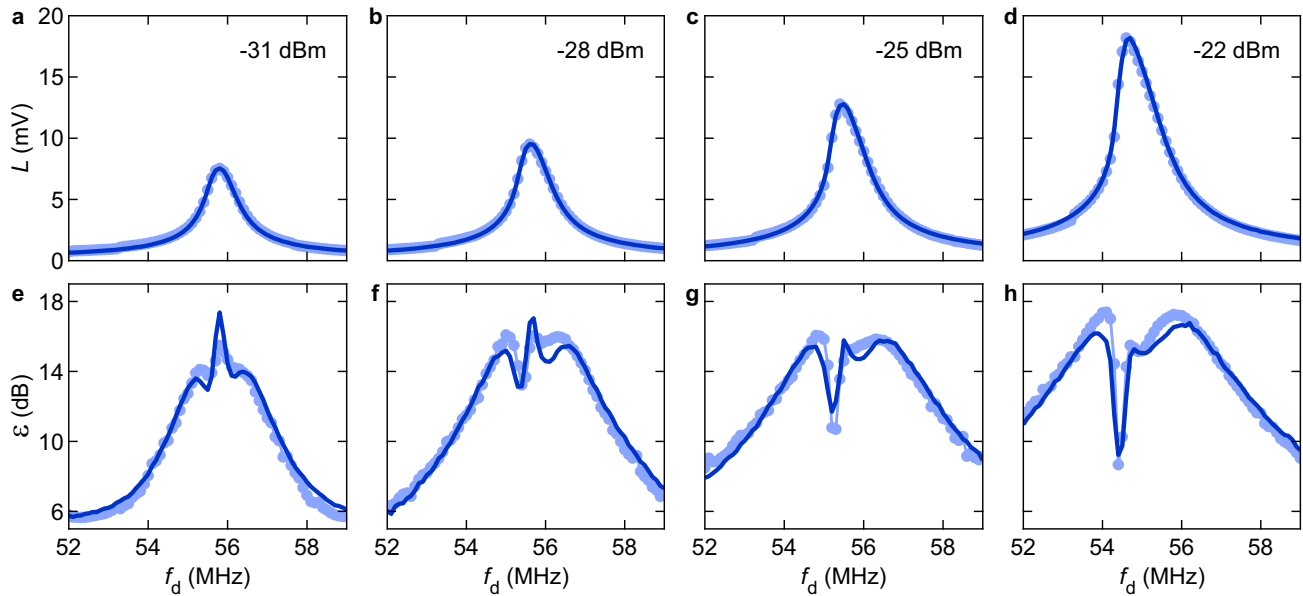


Fig. 2 | Nanomechanical response to a drive modulated with a video signal at a symbol rate $R_{\text{sym}} = 0.5 \times 10^6$ Hz. a–d Time-averaged vector length L of the discrete symbol components I_{out} and Q_{out} extracted from the output signal, plotted as a function of drive frequency f_d . The standard deviation of the measurements is ≈ 0.4 mV, which is comparable to the size of the dots. **e–h** Reciprocal of the error

vector magnitude, $\varepsilon(f_d)$, under the same conditions. Drive power at the gate is $P_d = -31$ dBm (**a, e**), -28 dBm (**b, f**), -25 dBm (**c, g**), and -22 dBm (**d, h**). Dots indicate measured data; solid lines are theoretical calculations. The gate voltage is $V_g^{\text{dc}} = 13$ V in all panels. Source data are provided as a Source Data file.

curves resemble broadened resonance peaks, the $\varepsilon(f_d)$ traces exhibit richer features. At low drive power, $\varepsilon(f_d)$ peaks near f_m and develops two local minima away from resonance (Fig. 2e), the latter being more pronounced at $R_p = 10^6$ Hz (Fig. 3e). At higher P_d , the local minimum in $\varepsilon(f_d)$ that appears where $|\partial L/\partial f_d|$ is largest deepens significantly, and the maxima in $\varepsilon(f_d)$ shift further from resonance (Figs. 2h and 3h). These extrema in $\varepsilon(f_d)$ are important features, as they directly affect the quality of the demodulated video.

Discussion

To understand these observations, we numerically solve the resonator's equation of motion in response to the multifrequency driving force $F_d(t)$. The equation reads^{63,64}:

$$\ddot{z} + \left[\frac{\omega_m}{Q_m} + \frac{\eta}{m_{\text{eff}}} z^2 \right] \dot{z} + \left[\omega_m^2 + \frac{\alpha}{m_{\text{eff}}} z^2 \right] z = \frac{F_d(t)}{m_{\text{eff}}}, \quad (1)$$

where z is the resonator displacement, $\omega_m = 2\pi f_m$ is the angular resonant frequency, η is the nonlinear damping coefficient, and α is the Duffing elastic constant. The values $Q_m \approx 100$, $\eta \approx 1.2 \times 10^5 \text{ kg m}^{-2} \text{ s}^{-1}$ and $\alpha \approx -10^{14} \text{ kg m}^{-2} \text{ s}^{-2}$ (arising from the electrical potential acting on the resonator, see ref. 65) are estimated from the response to a single-tone drive (Supplementary Note 5). The effective mass is estimated as $m_{\text{eff}} \approx 2 \times 10^{-17} \text{ kg}$ based on the resonator shape and the number of graphene layers. As in the experiment, the baseband signals $\tilde{I}_{\text{in}}(t)$ and $\tilde{Q}_{\text{in}}(t)$ that define $F_d(t)$ are computed from two streams of voltage pulses. The pulse amplitudes randomly take values $\pm V_{\text{in}}$ at a rate R_{sym} . These pulse streams are processed with a raised cosine (RC) filter (Fig. 1b). The use of this filter is justified, given that most of the measured noise appears at the receiver output. For completeness, we also consider the scenario where white Gaussian force noise is added at the drive stage, in addition to receiver noise. This case requires a cascade of two RRC filters: one at the transmitter and one at the receiver. However, we find that modeling receiver noise alone suffices to explain our measurements.

We demodulate $z(t)$ to obtain $\tilde{I}_{\text{out}}(t) = 2h(t) * [\xi z(t) \cos(2\pi f_d t)]$ and $\tilde{Q}_{\text{out}}(t) = 2h(t) * [\xi z(t) \sin(2\pi f_d t)]$, where h is a lowpass filter, ξ is a conversion factor in V m^{-1} , and $*$ denotes convolution. The symbol components I_{out} and Q_{out} are obtained by decimating $\tilde{I}_{\text{out}}(t)$ and $\tilde{Q}_{\text{out}}(t)$ at the symbol rate R_{sym} , accounting for the delay introduced by the RC filter. This simple model reproduces our measured $L(f_d)$ and $\varepsilon(f_d)$ traces (solid blue lines in Figs. 2 and 3). The only fit parameter in the analysis of $L(f_d)$ is $\xi \approx 7 \times 10^5 \text{ V m}^{-1}$. Notably, the lineshape of $L(f_d)$ is broader than that obtained with an unmodulated drive at the same P_d (Supplementary Note 2). To analyze $\varepsilon(f_d)$, we model fluctuations $\delta \tilde{I}_{\text{out}}$ and $\delta \tilde{Q}_{\text{out}}$ at the receiver output as additive white Gaussian noise with variance σ^2 . This noise contributes to the spread of the symbol clouds, leading to the modified expression $d^2 \rightarrow d^2 + (\delta \tilde{I}_{\text{out}}^2) + (\delta \tilde{Q}_{\text{out}}^2) = d^2 + 2\sigma^2$. We use $\sigma^2 \approx 3.9 \times 10^{-19} \text{ m}^2$ as a single fit parameter in the analysis of $\varepsilon(f_d)$. Measurements of the noise at the receiver output are presented in Supplementary Note 6.

Interestingly, the lineshape of $\varepsilon(f_d)$ near f_m is not influenced by the noise at the receiver. The parameter σ^2 is only required to capture the decay of $\varepsilon(f_d)$ away from f_m , and it has only a little incidence on the most interesting features that are the minima in $\varepsilon(f_d)$. To show this, in Fig. 3e–h we display our calculations for $\varepsilon(f_d)$ with no added noise, that is, without any fit parameter (orange traces). In this case, ε increases as f_d is stepped away from f_m , while the features near f_m remain similar to those in the presence of noise. This indicates that the spread of the symbol clouds, $d(f_d)$, near f_m is caused by a process other than noise.

This process is the loss of coherence in the response, resulting from the superposition of multifrequency vibrations with different amplitudes and phases. It is a hallmark of vibrations driven by a coherent, multifrequency signal and is not seen with single-tone drives or with force noise. It is caused by the resonator acting as a filter in the case where the spectrum of the drive is broader than the response, $W \gtrsim W_m$. If the drive were narrowband, $W \ll W_m$, the input symbol components ($I_{\text{in}}, Q_{\text{in}}$) would be transformed into ($I_{\text{out}}, Q_{\text{out}}$) by a simple rotation through the phase angle of the response. By contrast, each frequency component in the broadband drive is transduced into a

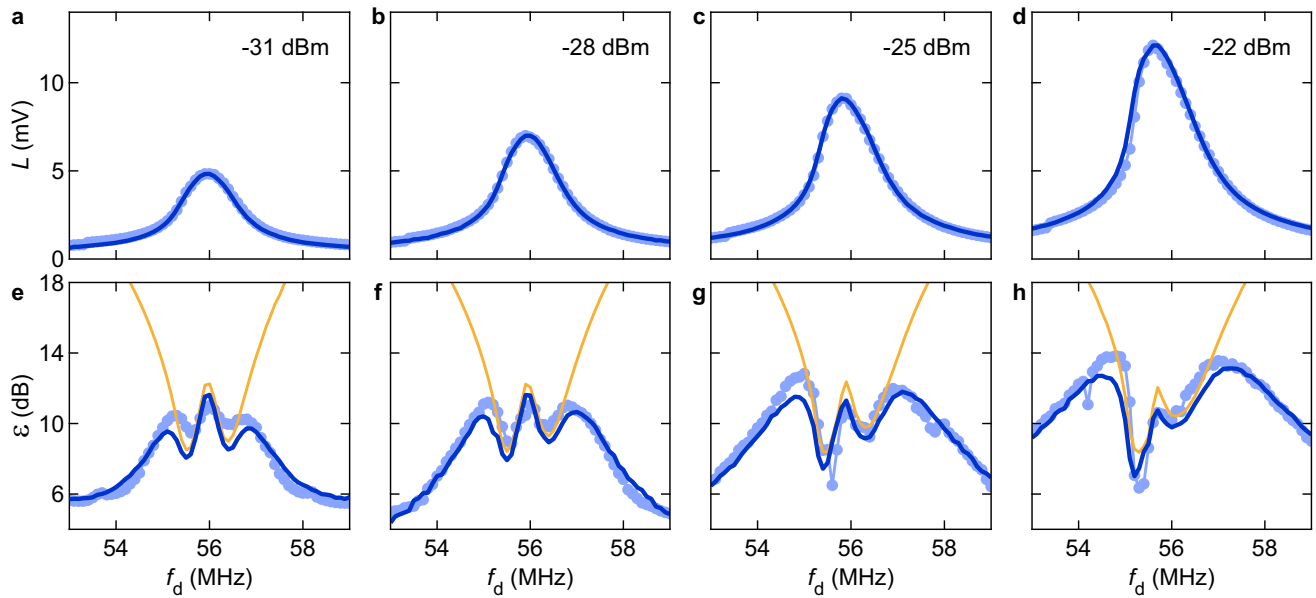


Fig. 3 | Nanomechanical response to a drive modulated with a video signal at a symbol rate $R_{\text{sym}} = 10^6$ Hz. a–d Time-averaged vector length L of the discrete symbol components I_{out} and Q_{out} as a function of drive frequency f_d . The standard deviation of the measurements is ≈ 0.4 mV, which is comparable to the size of the dots. **e–h** Reciprocal of the error vector magnitude, $\varepsilon(f_d)$. Drive power at the gate is

$P_d = -31$ dBm (**a, e**), -28 dBm (**b, f**), -25 dBm (**c, g**), and -22 dBm (**d, h**). Dots represent measured data [note: measurement noise in (**f**) is slightly higher than in (**e**), (**g**), and (**h**)]. Blue (orange) solid lines represent calculated traces with noise on (off). The gate voltage is $V_g^{\text{dc}} = 13$ V in all panels. Source data are provided as a Source Data file.

vibrational frequency component with a distinct amplitude and phase. Where f_d is far from f_m , and provided that receiver noise is low, $(I_{\text{out}}, Q_{\text{out}})$ still result from a simple rotation through a constant angle (≈ 0 or $-\pi$), since the magnitude and the phase of the response depend on frequency only weakly. In this case, $I_{\text{out}} \propto \pm I_{\text{in}}$ and $Q_{\text{out}} \propto \pm Q_{\text{in}}$. Where $f_d \approx f_m$, $W \approx W_m$, and where the response is linear (that is, at low P_d), we find $I_{\text{out}} \propto I_{\text{in}}$ and $Q_{\text{out}} \propto -I_{\text{in}}$ (Supplementary Note 7), meaning that input and output symbols are simply swapped. This has no adverse effect on video demodulation (Supplementary Note 8). However, the dephasing effect of the response on I_{out} and Q_{out} is strongest where $|f_d - f_m| \approx W/2$ and $W \geq W_m$. This case is depicted in Fig. 1c, d, where the upper frequency edge of the drive spectrum is near resonance and the lower frequency edge is far from it. There, $\tilde{I}_{\text{out}}(t)$ contains dephased frequency components from both $\tilde{I}_{\text{in}}(t)$ and $\tilde{Q}_{\text{in}}(t)$, and similarly for $\tilde{Q}_{\text{out}}(t)$ [Supplementary Note 7]. The fact that the in-phase component of the vibrations depends on both the in-phase and quadrature components of the drive, and that the quadrature response likewise depends on both drive components, can already be seen by solving Eq. (1) in the linear regime, yielding:

$$\begin{aligned} \tilde{I}_{\text{out}}(t) &\approx \frac{\kappa}{4m_{\text{eff}}\omega_d} \int_0^\infty dt' \exp(-\Gamma_m t') \left[-\tilde{I}_{\text{in}}(t-t') \sin \Delta\omega t' - \tilde{Q}_{\text{in}}(t-t') \cos \Delta\omega t' \right], \\ \tilde{Q}_{\text{out}}(t) &\approx \frac{\kappa}{4m_{\text{eff}}\omega_d} \int_0^\infty dt' \exp(-\Gamma_m t') \left[\tilde{I}_{\text{in}}(t-t') \cos \Delta\omega t' - \tilde{Q}_{\text{in}}(t-t') \sin \Delta\omega t' \right], \end{aligned} \quad (2)$$

where $\kappa = |\xi V_g^{\text{dc}} (1 + \Gamma) C_g'|$, $\omega_d = 2\pi f_d$, $\Gamma_m = \pi W_m$, and $\Delta\omega = 2\pi(f_d - f_m)$. As a result, decimating $\tilde{I}_{\text{out}}(t)$ and $\tilde{Q}_{\text{out}}(t)$ yields broad distributions of I_{out} and Q_{out} going through zero, which reduces ε . Experimentally, the condition of $|f_d - f_m| \approx W/2$ coincides with the minima observed in $\varepsilon(f_d)$ for $R_{\text{sym}} = 0.5 \times 10^6$ Hz and 10^6 Hz in the linear regime.

In the nonlinear regime (high P_d), our model also captures both the deepening of the local minimum (dip) in $\varepsilon(f_d)$ near the point of steepest slope in $L(f_d)$, and the frequency shift of the dip, Δf_{dip} , as P_d increases. In Supplementary Note 9, we show that Δf_{dip} is approximately proportional to the square of the change in vector length, ΔL_{dip} ,

that is, $\Delta f_{\text{dip}} \propto (\Delta L_{\text{dip}})^2$. This behavior is consistent with the quartic relationship between the frequency of a vibrational mode and the vibrational amplitude caused by weak conservative nonlinearities in the case where the mode is driven by a single tone drive^{66–68}. It is also consistent with the lineshape broadening of the mechanical response induced by the interplay between conservative nonlinearities and a force noise^{13,14,69}, as further detailed in Supplementary Note 9.

To complement our measurements of ε and directly quantify the effect of the mechanical response on the driving bit stream, we measure the bit error ratio (BER) of the nanomechanical transduction. This ratio represents the number of misread bits in the received stream (output bit stream) relative to the number of bits in the stream sent by the transmitter (input bit stream). Measuring BER is not straightforward because propagation and filtering delays complicate the direct comparison of the input and output bit streams. We solve this problem by inserting a marker at the beginning of the input bit stream. The marker consists of a train of bits '0' followed by a train of bits '1', which are easily identifiable on the receiver side. This enables a bit-by-bit comparison between the input and output streams. As an example, Fig. 4a shows a short input bit stream (hollow squares) and the corresponding received output bit stream (dots), obtained with $R_{\text{sym}} = 0.5 \times 10^6$ Hz. This example illustrates an error-free transduction, where BER = 0. Figures 4b–f present BER as a function of f_d , measured at $R_{\text{sym}} = 0.5 \times 10^6$ Hz (blue dots) and $R_{\text{sym}} = 10^6$ Hz (orange dots), spanning from the linear to the nonlinear regime [with increasing P_d from (b) to (f)]. At each f_d , BER is computed from a single 15-second measurement of the output bit stream. We find that BER at $R_{\text{sym}} = 0.5 \times 10^6$ Hz is consistently lower than at $R_{\text{sym}} = 10^6$ Hz, indicating that the minimum bit error ratio, BER_{min} , depends on R_{sym} . At the largest P_d and $R_{\text{sym}} = 0.5 \times 10^6$ Hz (Fig. 4f), we measure $\text{BER}_{\text{min}} \approx 5 \times 10^{-6}$, corresponding to 5 misread bits per million sent to the resonator. This limit is set by noise in our setup (Supplementary Notes 4 and 6). Furthermore, we observe that $\text{BER}(f_d)$ develops a sharp peak as P_d increases. This peak coincides with the emergence of the lower frequency dip in $\varepsilon(f_d)$ (Supplementary Note 9). At the peak frequency, the symbol clouds on the constellation diagram are strongly

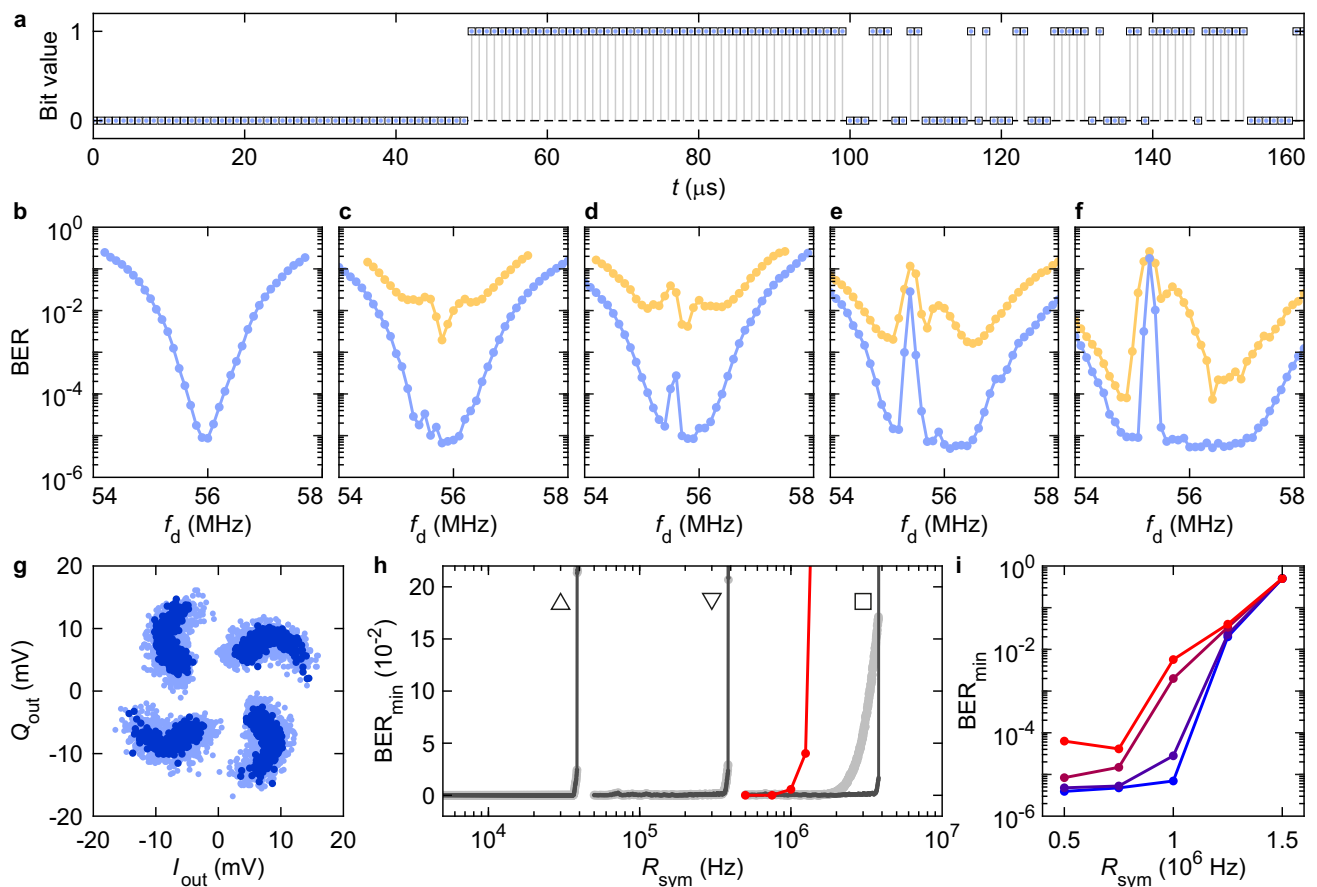


Fig. 4 | Bit error ratio (BER) of the nanomechanical transduction. **a** Bit stream at the transmitter (hollow squares) and at the receiver (dots), measured at $R_{\text{sym}} = 0.5 \times 10^6$ Hz. In 4-QAM, two bits form one symbol, so the bit rate is twice the symbol rate. **b–f** BER as a function of drive frequency f_d at $R_{\text{sym}} = 0.5 \times 10^6$ Hz (blue dots) and $R_{\text{sym}} = 10^6$ Hz (orange dots) for drive powers $P_d = -34$ dBm (**b**), -31 dBm (**c**), -28 dBm (**d**), -25 dBm (**e**), and -22 dBm (**f**). **g** Constellation diagram of I_{out} and Q_{out} at $P_d = -25$ dBm with f_d set to the BER peak frequency in (**e**). Light blue dots: measurements; dark blue dots: calculations. **h** Minimum BER in the linear

regime as a function of R_{sym} . Gray traces show calculations without (dark gray) and with (light gray) additive noise at the receiver. Upward triangle: $W_m = 10^4$ Hz; downward triangle: $W_m = 10^5$ Hz; square: $W_m = 10^6$ Hz. Red dots: measurements at $P_d = -28$ dBm. **i** Measured BER_{min} as a function of R_{sym} for different P_d values. From top (red) to bottom (blue): $P_d = -28$ dBm, -25 dBm, -22 dBm, -19 dBm. Measurements in (**h**, **i**) were performed in a noisier environment than those in (**b–g**). $V_g^{\text{dc}} = 13$ V in all panels. Source data are provided as a Source Data file.

distorted, as confirmed by our model (Fig. 4g), leading to decoding failure of the nanomechanical video. In Supplementary Note 10, we present our calculated $L(f_d)$, $\varepsilon(f_d)$, $\text{BER}(f_d)$, and constellation diagrams as an embedded animation to help visualize how these quantities relate to one another.

With regard to applications, we now examine the dependence of BER_{min} on R_{sym} . Our goal is to determine how R_{sym}^* , the highest symbol rate at which BER_{min} remains low, varies with the mechanical linewidth W_m . We interpret R_{sym}^* as the effective filtering bandwidth of the resonator for the video signal. We focus on BER at resonance in the linear regime, where $\text{BER}(f_d) = \text{BER}_{\text{min}}$ (Fig. 4b). In Fig. 4h, we plot BER_{min} as a function of R_{sym} , calculated using Eq. (1) for $W_m = 10^4$ Hz, 10^5 Hz, and 10^6 Hz (gray traces, from left to right). The dark traces correspond to calculations without noise, while the light traces include additive Gaussian noise with variance σ^2 , as used in Figs. 2 and 3. Each trace computed without noise exhibits a kink near $R_{\text{sym}} \approx 3.5W_m$, which sets an upper bound for R_{sym}^* . When noise is added, R_{sym}^* shifts to lower values, particularly for larger W_m (that is, lower Q_m), as $\text{BER}_{\text{min}}(R_{\text{sym}})$ begins to increase at lower symbol rates. The red dots in Fig. 4h represent measured values of $\text{BER}_{\text{min}}(R_{\text{sym}})$, obtained at $P_d = -28$ dBm, near the onset of the nonlinear regime and in the presence of noise. From these data, we extract an experimental filtering bandwidth of $R_{\text{sym}}^* \approx 10^6$ Hz. Additional measurements of BER_{min} across a range of P_d

are shown in Fig. 4i (see also Supplementary Note 11). As expected, these results indicate that nanomechanical information encoding suffers less information loss at higher drive powers.

We now demonstrate the filtering and video encoding capabilities of our resonator. Figure 5a shows that the nanomechanical response (measured here using a single-tone drive) depends on the gate voltage V_g^{dc} . Since both ε and BER strongly depend on $|f_m - f_d|$, we can transmit multiple videos with well separated f_d simultaneously, and selectively demodulate one of them by appropriately tuning f_m with V_g^{dc} . Our experimental setup for broadcasting two videos in parallel is illustrated in Fig. 5b. Two SDR transmitters are used: one operating at $f_d = 57.8 \times 10^6$ Hz = f_A , and the other at $f_d = 60.8 \times 10^6$ Hz = f_B . Both transmitters are configured with $R_p = 10^6$ Hz and $P_d = -22$ dBm, a power at which the resonator responds nonlinearly. The drive frequencies are chosen to avoid the dip in $\varepsilon(f_d)$. Figure 5c shows $\dot{I}_{\text{out}}(t)$ and $Q_{\text{out}}(t)$, with V_g^{dc} initially set to 14 V and the receiver's center frequency f_r set to f_A at $t = 0$. Between $t = 17$ s and $t = 19$ s, V_g^{dc} is ramped from 14 V to 15 V, and f_r is set in software to f_B . Then, between $t = 40$ s and $t = 42$ s, V_g^{dc} is ramped back down from 15 V to 14 V, and f_r is reset to f_A . Figure 5c shows that the desired broadcast, A or B, can be selected by adjusting V_g^{dc} .

In the spirit of previous nanomechanical devices used as signal processors³⁹, we envision that our FLG resonators, as well as other

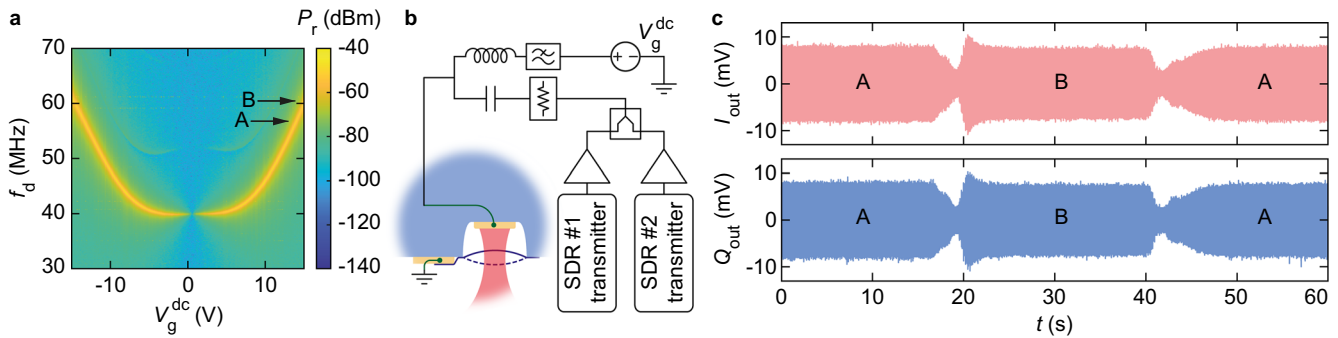


Fig. 5 | Multichannel nanomechanical television broadcast. **a** Response of the resonator to a single-tone drive as a function of gate voltage V_g^{dc} and drive frequency f_d , at a drive power $P_d = -40$ dBm. The arrows show the two operating points (V_g^{dc}, f_d), each of which defines the carrier frequency for one of the video signals (A or B). **b** Experimental setup featuring two software-defined radios

transmitting in parallel; a single receiver is used. **c** $\bar{I}_{out}(t)$ and $\bar{Q}_{out}(t)$ components of the baseband output signal. Received video A ($0\text{ s} < t < 17\text{ s}$): $V_g^{dc} = 14\text{ V}$, receiver center frequency $f_r = 57.8 \times 10^6\text{ Hz}$. Received video B ($19\text{ s} < t < 40\text{ s}$): $V_g^{dc} = 15\text{ V}$, $f_r = 60.8 \times 10^6\text{ Hz}$. Received video A ($t > 42\text{ s}$): $V_g^{dc} = 14\text{ V}$, $f_r = 57.8 \times 10^6\text{ Hz}$. Source data are provided as a Source Data file.

resonators based on similar principles, may serve as passive radio receivers operating in the HF and VHF bands of the radio spectrum. With a resonant frequency ranging from $\approx 40 \times 10^6\text{ Hz}$ to $\approx 60 \times 10^6\text{ Hz}$ (Fig. 5a), our resonator operates within the 6-meter subband, which is internationally allocated for amateur radio use. In this subband, digital amateur television (DATV) broadcasts have been conducted using signals with a 300 kHz bandwidth⁴⁹. In the United Kingdom, DATV with a broader bandwidth of up to 500 kHz is permitted in the 2-meter amateur radio band (144–148 MHz)⁴⁹. Smaller-diameter FLG resonators, or higher-order vibrational modes, can operate in this frequency range. The filtering bandwidth of our resonator, along with the maximum 4-QAM data rate of its transduction, $2R_{sym}^* \approx 2 \times 10^6\text{ bps}$, is fully compatible with DATV.

While our experimental setup may not yet be practical for receiving amateur radio broadcasts, it can be further simplified⁵¹. The resonator would serve a dual purpose: as a front-end, tunable band-pass filter, and as a passive optocoupler. It could be placed at the output of the preamplifier that is typically connected to the feedpoint of a receiving antenna⁷⁰. As a filter, it would reject jamming and other interfering signals in a manner similar to surface acoustic wave filters, but with the added benefit of a tunable center frequency, and without the fabrication complexity of more advanced tunable front-end filters⁷¹. As an optocoupler, it would passively convert the radio signal into modulations of reflected light intensity through the nanomechanical transduction, effectively eliminating the issue of radio frequency interference caused by common-mode currents in the coaxial cable that connects the antenna to the demodulator⁷⁰. The detection of weaker radio signals may be improved by using more advanced SDR systems with lower receiver noise and by engineering the mirror underneath the resonator to enhance the responsivity of the device⁷². Admittedly, the idea of using nanomechanical resonators for radio communication remains largely academic due to challenges related to device reproducibility and thermal drift⁴⁰. Nevertheless, these resonators may eventually enable alternative architectures for shortwave radio receivers, facilitating the decoding of images and videos carried by weak signals in noisy environments⁶¹.

Methods

Optical detection of vibrations

The incident light is provided by a Helium-Neon laser operating at a wavelength of $\lambda = 633\text{ nm}$. The laser output is coupled into a single-mode optical fiber for spatial filtering. A half-wave plate sets the linear polarization of the emerging light, which then passes through a quarter-wave plate to become circularly polarized. The circularly polarized beam is focused onto the resonator with an aspheric lens and reflected by the

gate electrode, acting as a mirror. After traversing the quarter-wave plate again, the reflected beam emerges linearly polarized, orthogonal to the incident polarization. A polarizing beam splitter separates the incident and reflected beams, directing the reflected light to the photodetector (Thorlabs APD430A2 avalanche photodetector). As a function of time t , the voltage at the output of the photodetector reads:

$$v(t) \approx P_{inc} \frac{\partial \mathcal{R}}{\partial z_s} \Big|_{z_s} \delta z(t) * \psi(t) + \delta v_b, \quad (3)$$

where $P_{inc} \approx 3 \times 10^{-6}\text{ W}$ is the optical power incident on the resonator, \mathcal{R} is the optical reflectance of the device composed of the resonator, the gate electrode, and the vacuum gap between them, δz is the vibrational amplitude of the resonator (that is, its dynamic displacement), z_s is the static displacement of the resonator, $|\partial \mathcal{R} / \partial z|_{z_s} \approx 3 \times 10^6\text{ m}^{-1}$ is the calculated optical responsivity of the device⁵², ψ is the response function of the photodetector in units of $\text{V W}^{-1}\text{ s}^{-1}$, δv_b is a background voltage noise, and $*$ denotes convolution.

Driving voltage and driving force waveforms

To build the driving voltage and the driving force waveforms, we start with two streams of pulses $p_k = \pm 1$ and $q_k = \pm 1$, generated at a pulse (symbol) rate R_{sym} . The streams are filtered using either a raised cosine (RC) filter or a root raised cosine (RRC) filter, yielding waveforms $\tilde{p}(t)$ and $\tilde{q}(t)$ that vary continuously in time t . Where noise is added to the signal after the transmitter and before the receiver, an RRC filter is applied at the transmitter to shape the pulses, and a second RRC filter is applied at the receiver to filter the baseband signal. The cascade of these two RRC filters is equivalent to a single RC filter and serves to minimize intersymbol interference, just as a single RC filter does in a noiseless scenario. The waveforms $\tilde{p}(t)$ and $\tilde{q}(t)$ can be expressed as:

$$\tilde{p}(t) = \sum_{k=0}^{\infty} p_k g(t - kT_{sym}), \quad \tilde{q}(t) = \sum_{k=0}^{\infty} q_k g(t - kT_{sym}), \quad (4)$$

where g is the impulse response of the filter and T_{sym} is the reciprocal of the symbol rate, $T_{sym} = 1/R_{sym}$. For a RC filter, g reads:

$$g(t) = \frac{\pi}{4T_{sym}} \text{sinc}\left(\frac{t}{2\beta}\right) \quad \text{if } t = \pm \frac{T_{sym}}{2\beta} \quad (5)$$

$$g(t) = \frac{1}{T_{sym}} \text{sinc}\left(\frac{t}{T_{sym}}\right) \frac{\cos\left(\frac{\pi\beta t}{T_{sym}}\right)}{1 - \left(\frac{2\beta t}{T_{sym}}\right)^2} \quad \text{otherwise,} \quad (6)$$

where β is the roll-off factor of the filter. The filtered pulses are used to modulate the amplitude of the in-phase component and that of the quadrature component of the waveform $x(t)$ defined as:

$$x(t) = \bar{p}(t) \cos(\omega_d t) + \bar{q}(t) \sin(\omega_d t), \quad (7)$$

where ω_d is the angular frequency of the drive. Given a peak voltage amplitude V_{in} , the driving voltage waveform $s(t)$ is defined as:

$$s(t) = V_{in} x(t) = \bar{I}_{in}(t) \cos(\omega_d t) + \bar{Q}_{in}(t) \sin(\omega_d t), \quad (8)$$

where $\bar{I}_{in}(t)$ and $\bar{Q}_{in}(t)$ are the baseband in-phase and quadrature components of the drive, respectively. They are defined as:

$$\bar{I}_{in}(t) = V_{in} \bar{p}(t), \quad \bar{Q}_{in}(t) = V_{in} \bar{q}(t). \quad (9)$$

The power of $s(t)$ that would be dissipated across a 50 Ohm resistor in units of dBm is:

$$P_{in} = 10 \log_{10} \left(\frac{\langle s^2(t) \rangle}{50 \times 10^{-3}} \right) = 10 \log_{10} \left(\frac{V_{in}^2 \langle x^2(t) \rangle}{50 \times 10^{-3}} \right), \quad (10)$$

where $\langle \cdot \rangle$ averages over time. Hence, the peak voltage V_{in} reads:

$$V_{in} = \left(\frac{10^{P_{in}/10} \times 50 \times 10^{-3}}{\langle x^2(t) \rangle} \right)^{1/2}. \quad (11)$$

The total voltage between the gate and the resonator is the total voltage of the standing wave at the gate:

$$V_d = (1 + \Gamma) V_{in}, \quad (12)$$

where $\Gamma \simeq 1$ is the reflection coefficient of $s(t)$ at the gate. The equivalent driving power that would be dissipated across a 50 Ohm resistor in units of dBm is then:

$$P_d = 10 \log_{10} \left[\frac{(1 + \Gamma)^2 \langle s^2(t) \rangle}{50 \times 10^{-3}} \right] = 20 \log_{10}(1 + \Gamma) + P_{in} \simeq 6 + P_{in}. \quad (13)$$

The driving force waveform reads:

$$F_d(t) = |V_g^{dc}| (1 + \Gamma) \left| \frac{dC_g}{dz} \right| s(t), \quad (14)$$

where V_g^{dc} is the dc voltage applied between the resonator and the gate, and dC_g/dz is the derivative with respect to the displacement of the resonator of the capacitance between the resonator and the gate.

Data availability

The data used in this study are available at <https://doi.org/10.5281/zenodo.17150504>. Source data are provided with this paper.

Code availability

The codes used in this study are available at <https://doi.org/10.5281/zenodo.17150778>.

References

- Lemme, M. C. et al. Nanoelectromechanical sensors based on suspended 2D materials. *Research* **2020**, 1–25 (2020).
- Xu, B. et al. Nanomechanical resonators: Toward atomic scale. *ACS Nano* **16**, 15545–15585 (2022).
- Bachtold, A., Moser, J. & Dykman, M. I. Mesoscopic physics of nanomechanical systems. *Rev. Mod. Phys.* **94**, <https://doi.org/10.1103/RevModPhys.94.045005> (2022).
- Schmid, S., Villanueva, L. G. & Roukes, M. L. *Fundamentals of Nanomechanical Resonators* (Second Edition, 2023).
- Nathanson, H. C., Newell, W. E., Wickstrom, R. A. & Davis, J. R. The resonant gate transistor. *IEEE Trans. Electron Devices* **14**, 117–133 (1967).
- Sazonova, V. et al. A tunable carbon nanotube electromechanical oscillator. *Nature* **431**, 284–287 (2004).
- Unterreithmeier, Q. P., Weig, E. M. & Kotthaus, J. P. Universal transduction scheme for nanomechanical systems based on dielectric forces. *Nature* **458**, 1001–1004 (2009).
- Goldsche, M. et al. Fabrication of comb-drive actuators for straining nanostructured suspended graphene. *Nanotechnology* **29**, <https://doi.org/10.1088/1361-6528/aacdec> (2018).
- Singh, V. et al. Probing thermal expansion of graphene and modal dispersion at low-temperature using graphene nanoelectromechanical systems resonators. *Nanotechnology* **21**, <https://doi.org/10.1088/0957-4484/21/16/165204> (2010).
- Chiout, A. et al. Extreme mechanical tunability in suspended MoS₂ resonator controlled by Joule heating. *NPJ 2D Mater. Appl.* **7**, <https://doi.org/10.1038/s41699-023-00383-3> (2023).
- Stambaugh, C. & Chan, H. B. Noise activated switching in a driven, nonlinear micromechanical oscillator. *Phys. Rev. B* **73**, <https://doi.org/10.1103/PhysRevB.73.172302> (2006).
- Zhang, Y. & Dykman, M. I. Spectral effects of dispersive mode coupling in driven mesoscopic systems. *Phys. Rev. B* **92**, <https://doi.org/10.1103/PhysRevB.92.165419> (2015).
- Maillet, O. et al. Nonlinear frequency transduction of nanomechanical Brownian motion. *Phys. Rev. B* **96**, <https://doi.org/10.1103/PhysRevB.96.165434> (2017).
- Huang, L. et al. Frequency stabilization and noise-induced spectral narrowing in resonators with zero dispersion. *Nat. Commun.* **10**, <https://doi.org/10.1038/s41467-019-11946-8> (2019).
- Dykman, M. I., Khasin, M., Portman, J. & Shaw, S. W. Spectrum of an oscillator with jumping frequency and the interference of partial susceptibilities. *Phys. Rev. Lett.* **105**, <https://doi.org/10.1103/PhysRevLett.105.230601> (2010).
- Siria, A. et al. Electron fluctuation induced resonance broadening in nano electromechanical systems: The origin of shear force in vacuum. *Nano Lett.* **12**, 3551–3556 (2012).
- Fong, K. Y., Pernice, W. H. P. & Tang, H. X. Frequency and phase noise of ultrahigh Q silicon nitride nanomechanical resonators. *Phys. Rev. B* **85**, <https://doi.org/10.1103/PhysRevB.85.161410> (2012).
- Zhang, Y., Moser, J., Güttinger, J., Bachtold, A. & Dykman, M. I. Interplay of driving and frequency noise in the spectra of vibrational systems. *Phys. Rev. Lett.* **113**, <https://doi.org/10.1103/PhysRevLett.113.255502> (2014).
- Sun, F., Zou, J., Maizelis, Z. A. & Chan, H. B. Telegraph frequency noise in electromechanical resonators. *Phys. Rev. B* **91**, <https://doi.org/10.1103/PhysRevB.91.174102> (2015).
- Kalaei, M. et al. Quantum electromechanics of a hypersonic crystal. *Nat. Nanotechnol.* **14**, 334–339 (2019).
- Chen, C. et al. Performance of monolayer graphene nanomechanical resonators with electrical readout. *Nat. Nanotechnol.* **4**, 861–867 (2009).
- Nichol, J. M., Hemesath, E. R., Lauhon, L. J. & Budakian, R. Nanomechanical detection of nuclear magnetic resonance using a silicon nanowire oscillator. *Phys. Rev. B* **85**, <https://doi.org/10.1103/PhysRevB.85.054414> (2012).
- Gouttenoire, V. et al. Digital and FM demodulation of a doubly clamped single-walled carbon-nanotube oscillator: Towards a nanotube cell phone. *Small* **6**, 1060–1065 (2010).
- Westra, H.J.R., Poot, M., van der Zant, H.S.J. & Venstra, W. J. Nonlinear Modal Interactions in Clamped-Clamped Mechanical Resonators. *Phys. Rev. Lett.* **105**, <https://doi.org/10.1103/PhysRevLett.105.117205> (2010).

25. Dykman, M. I. Heating and cooling of local and quasilocal vibrations by nonresonance field. *Sov. Phys. Solid State* **20**, 1306–1311 (1978).
26. Mahboob, I., Nishiguchi, K., Okamoto, H. & Yamaguchi, H. Phonon-cavity electromechanics. *Nat. Phys.* **8**, 387–392 (2012).
27. De Alba, R. et al. Tunable phonon-cavity coupling in graphene membranes. *Nat. Nanotechnol.* **11**, 741–746 (2016).
28. Mathew, J. P., Patel, R. N., Borah, A., Vijay, R. & Deshmukh, M. M. Dynamical strong coupling and parametric amplification of mechanical modes of graphene drums. *Nat. Nanotechnol.* **11**, 747–751 (2016).
29. Dong, X., Dykman, M. I. & Chan, H. B. Strong negative nonlinear friction from induced two-phonon processes in vibrational systems. *Nat. Commun.* **9**, <https://doi.org/10.1038/s41467-018-05246-w> (2018).
30. Ryvkine, D. & Dykman, M. I. Resonant symmetry lifting in a parametrically modulated oscillator. *Phys. Rev. E* **74**, <https://doi.org/10.1103/PhysRevE.74.061118> (2006).
31. Mahboob, I., Froitier, C. & Yamaguchi, H. A symmetry breaking electromechanical detector. *Appl. Phys. Lett.* **96**, <https://doi.org/10.1063/1.3429589> (2010).
32. Leuch, A. et al. Parametric symmetry breaking in a nonlinear resonator. *Phys. Rev. Lett* **117**, <https://doi.org/10.1103/PhysRevLett.117.214101> (2016).
33. Erbe, A. et al. Mechanical mixing in nonlinear nanomechanical resonators. *Appl. Phys. Lett.* **77**, 3102–3104 (2000).
34. Jaber, N., Ramini, A. & Younis, M. I. Multifrequency excitation of a clamped-clamped microbeam: Analytical and experimental investigation. *Microsyst. Nanoeng.* **2**, <https://doi.org/10.1038/micronano.2016.2> (2016).
35. Mahboob, I., Flurin, E., Nishiguchi, K., Fujiwara, A. & Yamaguchi, H. Interconnect-free parallel logic circuits in a single mechanical resonator. *Nat. Commun.* **2**, <https://doi.org/10.1038/ncomms1201> (2011).
36. Ochs, J. S., Seitner, M., Dykman, M. I. & Weig, E. M. Amplification and spectral evidence of squeezing in the response of a strongly driven nanoresonator to a probe field. *Phys. Rev. A* **103**, <https://doi.org/10.1103/PhysRevA.103.013506> (2021).
37. Houri, S., Ohta, R., Asano, M., Blanter, Y. M. & Yamaguchi, H. Pulse-width modulated oscillations in a nonlinear resonator under two-tone driving as a means for MEMS sensor readout. *Jpn. J. Appl. Phys.* **58**, <https://doi.org/10.7567/1347-4065/aaffb9> (2019).
38. Catalini, L. et al. Slow and fast topological dynamical phase transitions in a Duffing resonator driven by two detuned tones. *Phys. Rev. Res.* **7**, 033058 (2025).
39. Nguyen, C. T.-C. Radios with micromachined resonators. *IEEE Spectrum* <https://spectrum.ieee.org/radios-with-micromachined-resonators> (2009).
40. Nguyen, C. T.-C. MEMS-based RF channel selection for true software-defined cognitive radio and low-power sensor communications. *IEEE Commun. Mag.* **51**, 110–119 (2013).
41. Jensen, K., Weldon, J., Garcia, H. & Zettl, A. Nanotube radio. *Nano Lett.* **7**, 3508–3511 (2007).
42. Rutherglen, C. & Burke, P. Carbon nanotube radio. *Nano Lett.* **7**, 3296–3299 (2007).
43. Zhou, Q., Zheng, J., Onishi, S., Crommie, M. F. & Zettl, A. K. Graphene electrostatic microphone and ultrasonic radio. *Proc. Natl. Acad. Sci. USA* **112**, 8942–8946 (2015).
44. Bartsch, S. T., Rusu, A. & Ionescu, A. M. A single active nanoelectromechanical tuning fork front-end radio-frequency receiver. *Nanotechnology* **23**, <https://doi.org/10.1088/0957-4484/23/22/225501> (2012).
45. Chen, C. et al. Graphene mechanical oscillators with tunable frequency. *Nat. Nanotechnol.* **8**, 923–927 (2013).
46. Rocheleau, T. O., Naing, T. L., Nilchi, J. N. & Nguyen, C. T.-C. A MEMS-based tunable RF channel-selecting super-regenerative transceiver for wireless sensor nodes. *Tech. Digest* **12**, 83–86 (2014).
47. Naing, T. L., Rocheleau, T. O. & Nguyen, C. T.-C. Simultaneous multifrequency switchable oscillator and FSK modulator based on a capacitive-gap MEMS disk array. In the *8th IEEE International Conference on Micro Electro Mechanical Systems (MEMS)* (2015).
48. Wang, J., Ding, G. & Wang, H. HF Communications: Past, present, and future. *China Commun.* **15**, 1–9 (2018).
49. Radio Society of Great Britain. Amateur television. <https://rsgb.org/main/technical/amateur-television/> (1913).
50. Haupt, F., Imamoglu, A. & Kroner, M. Single quantum dot as an optical thermometer for millikelvin temperatures. *Phys. Rev. Appl.* **2**, <https://doi.org/10.1103/PhysRevApplied.2.024001> (2014).
51. Lu, H. Imaging vibrations of electromechanical few layer graphene resonators with a moving vacuum enclosure. *Precis. Eng.* **72**, 769–776 (2021).
52. Zhang, C. et al. Graphene nanomechanical vibrations measured with a phase-coherent software-defined radio. *Comms. Eng.* **3**, <https://doi.org/10.1038/s44172-024-00186-4> (2024).
53. Bunch, J. S. et al. Electromechanical resonators from graphene sheets. *Science* **315**, 490–493 (2007).
54. Barton, R. A. et al. Photothermal self-oscillation and laser cooling of graphene optomechanical systems. *Nano Lett.* **12**, 4681–4686 (2012).
55. Davidovikj, D. et al. Visualizing the motion of graphene nanodrums. *Nano Lett.* **16**, 2768–2773 (2016).
56. Chen, H. et al. Gate-tunable bolometer based on strongly coupled graphene mechanical resonators. *Opt. Lett.* **48**, 81–84 (2023).
57. GNU Radio. <https://www.gnuradio.org> (2024).
58. HackRF software-defined radio transceiver. NESDR radio receiver. <https://www.nooelec.com/store/sdr/sdr-receivers/nesdr.html> (2024).
59. Franks, L. E. Carrier and bit synchronization in data communication - a tutorial review. *IEEE Trans. Commun.* **28**, 1107–1121 (1980).
60. Harris, F. J. & Rice, M. Multirate digital filters for symbol timing synchronization in software defined radios. *IEEE J. Sel. Areas Commun.* **19**, 2346–2357 (2001).
61. Crockett, L. H., Northcote, D. & Stewart, R. W. (Editors). *Software Defined Radio with Zynq UltraScale+ RFSoc* (First Edition, 2023).
62. FFmpeg. <https://ffmpeg.org> (2024).
63. Dykman, M. I. & Krivoglaз, M. A. Spectral distribution of nonlinear oscillators with nonlinear friction due to a medium. *Phys. Status Solidi B* **68**, 111–123 (1975).
64. Zaitsev, S., Shtempluck, O., Buks, E. & Gottlieb, O. Nonlinear damping in a micromechanical oscillator. *Nonlinear Dyn.* **67**, 859–883 (2012).
65. Lifshitz, R. & Cross, M. C. Nonlinear dynamics of nanomechanical and micromechanical resonators. in *Reviews of Nonlinear Dynamics and Complexity* (Wiley-VCH, 2008).
66. Carr, D. W., Evoy, S., Sekaric, L., Craighead, H. G. & Parpia, J. M. Measurement of mechanical resonance and losses in nanometer scale silicon wires. *Appl. Phys. Lett.* **75**, 920–922 (1999).
67. Husain, A. et al. Nanowire-based very-high-frequency electromechanical resonator. *Appl. Phys. Lett.* **83**, 1240–1242 (2003).
68. Kozinsky, I., Postma, H. W. Ch., Bargatin, I. & Roukes, M. L. Tuning nonlinearity, dynamic range, and frequency of nanomechanical resonators. *Appl. Phys. Lett.* **88**, <https://doi.org/10.1063/1.2209211> (2006).
69. Dykman, M. I. & Krivoglaз, M. A. Classical theory of nonlinear oscillators interacting with a medium. *Phys. Status Solidi B* **48**, 497–512 (1971).
70. ARRL—The National Association for Amateur Radio. *The ARRL Antenna Book for Radio Communications* (24th Ed, 2019).

71. Hashimoto, K.-Y. et al. Moving tunable filters forward. *IEEE Microw. Mag.* **16**, 89–97 (2015).
72. Lu, H. et al. Force sensing with a graphene nanomechanical resonator coupled to photonic crystal guided resonances. Preprint at <https://doi.org/10.48550/arXiv.2507.06755> (2025).

Acknowledgements

This work was supported by the National Natural Science Foundation of China (grant numbers 62150710547 and 62074107) and the project of the Priority Academic Program Development (PAPD) of Jiangsu Higher Education Institutions. The authors are grateful to Prof. Wang Chinhua for his strong support. J.M. is grateful to Dr. Martin Kroner for his advice on the optical measurement setup and on the flexible transmission lines. J.M. is grateful to Jean-François Moser for his help with FFmpeg.

Author contributions

C.Z. and J.M. assembled the data acquisition system. H.L., C.Y., and Y.Z. fabricated the nanomechanical devices with the help of F.C. H.L. built the optical setup with the help of Y.Y. C.Z. performed the measurements. J.M. conceived the experiment, analyzed the data, wrote the manuscript and the Supplementary Information, and supervised the work.

Competing interests

The authors declare no competing interests.

Additional information

Supplementary information The online version contains supplementary material available at <https://doi.org/10.1038/s41467-025-65550-0>.

Correspondence and requests for materials should be addressed to Heng Lu or Joel Moser.

Peer review information *Nature Communications* thanks Ying Cheng and the other anonymous reviewer(s) for their contribution to the peer review of this work. A peer review file is available.

Reprints and permissions information is available at <http://www.nature.com/reprints>

Publisher's note Springer Nature remains neutral with regard to jurisdictional claims in published maps and institutional affiliations.

Open Access This article is licensed under a Creative Commons Attribution-NonCommercial-NoDerivatives 4.0 International License, which permits any non-commercial use, sharing, distribution and reproduction in any medium or format, as long as you give appropriate credit to the original author(s) and the source, provide a link to the Creative Commons licence, and indicate if you modified the licensed material. You do not have permission under this licence to share adapted material derived from this article or parts of it. The images or other third party material in this article are included in the article's Creative Commons licence, unless indicated otherwise in a credit line to the material. If material is not included in the article's Creative Commons licence and your intended use is not permitted by statutory regulation or exceeds the permitted use, you will need to obtain permission directly from the copyright holder. To view a copy of this licence, visit <http://creativecommons.org/licenses/by-nc-nd/4.0/>.

© The Author(s) 2025